

## On the relative intensity of Poisson's spot

This content has been downloaded from IOPscience. Please scroll down to see the full text.

2017 New J. Phys. 19 033022

(<http://iopscience.iop.org/1367-2630/19/3/033022>)

View [the table of contents for this issue](#), or go to the [journal homepage](#) for more

Download details:

IP Address: 129.13.72.198

This content was downloaded on 10/07/2017 at 09:57

Please note that [terms and conditions apply](#).

You may also be interested in:

[Particle-wave discrimination in Poisson spot experiments](#)

T Reisinger, G Bracco and B Holst

[Photon field and energy flow lines behind a circular disc](#)

D Arsenovi, D Dimic and M Boži

[ANALYTIC MODELING OF STARSHADES](#)

Webster Cash

[Experimental methods of molecular matter-wave optics](#)

Thomas Juffmann, Hendrik Ulbricht and Markus Arndt

[Rayleigh--Sommerfeld diffraction and Poisson's spot](#)

Robert L Lucke

[A micromechanical optical switch with a zone-plate reflector](#)

Dennis S Greywall

[Super-resolution microscopy of single atoms in optical lattices](#)

Andrea Alberti, Carsten Robens, Wolfgang Alt et al.

[Hands-on Fourier analysis by means of far-field diffraction](#)

Nicolo' Giovanni Ceffa, Maddalena Collini, Laura D'Alfonso et al.

[Optimizing Fourier filtering for digital holographic particle image velocimetry](#)

Thomas Ooms, Wouter Koek, Joseph Braat et al.



## PAPER

## On the relative intensity of Poisson's spot

## OPEN ACCESS

## RECEIVED

16 November 2016

## REVISED

17 January 2017

## ACCEPTED FOR PUBLICATION

6 February 2017

## PUBLISHED

13 March 2017

T Reisinger<sup>1</sup>, P M Leufke, H Gleiter and H Hahn

Institute of Nanotechnology, Karlsruhe Institute of Technology, Hermann-von-Helmholtz-Platz 1, D-76344 Eggenstein-Leopoldshafen, Germany

<sup>1</sup> Author to whom any correspondence should be addressed.E-mail: [treisinger@gmail.com](mailto:treisinger@gmail.com)**Keywords:** spot of Arago, Fresnel diffraction, surface corrugation, Poisson's spot, Fresnel–KirchhoffSupplementary material for this article is available [online](#)

Original content from this work may be used under the terms of the [Creative Commons Attribution 3.0 licence](#).

Any further distribution of this work must maintain attribution to the author(s) and the title of the work, journal citation and DOI.

**Abstract**

The Fresnel diffraction phenomenon referred to as Poisson's spot or spot of Arago has, beside its historical significance, become relevant in a number of fields. Among them are for example fundamental tests of the super-position principle in the transition from quantum to classical physics and the search for extra-solar planets using star shades. Poisson's spot refers to the positive on-axis wave interference in the shadow of any spherical or circular obstacle. While the spot's intensity is equal to the undisturbed field in the plane wave picture, its intensity in general depends on a number of factors, namely the size and wavelength of the source, the size and surface corrugation of the diffraction obstacle, and the distances between source, obstacle and detector. The intensity can be calculated by solving the Fresnel–Kirchhoff diffraction integral numerically, which however tends to be computationally expensive. We have therefore devised an analytical model for the on-axis intensity of Poisson's spot relative to the intensity of the undisturbed wave field and successfully validated it both using a simple light diffraction setup and numerical methods. The model will be useful for optimizing future Poisson-spot matter-wave diffraction experiments and determining under what experimental conditions the spot can be observed.

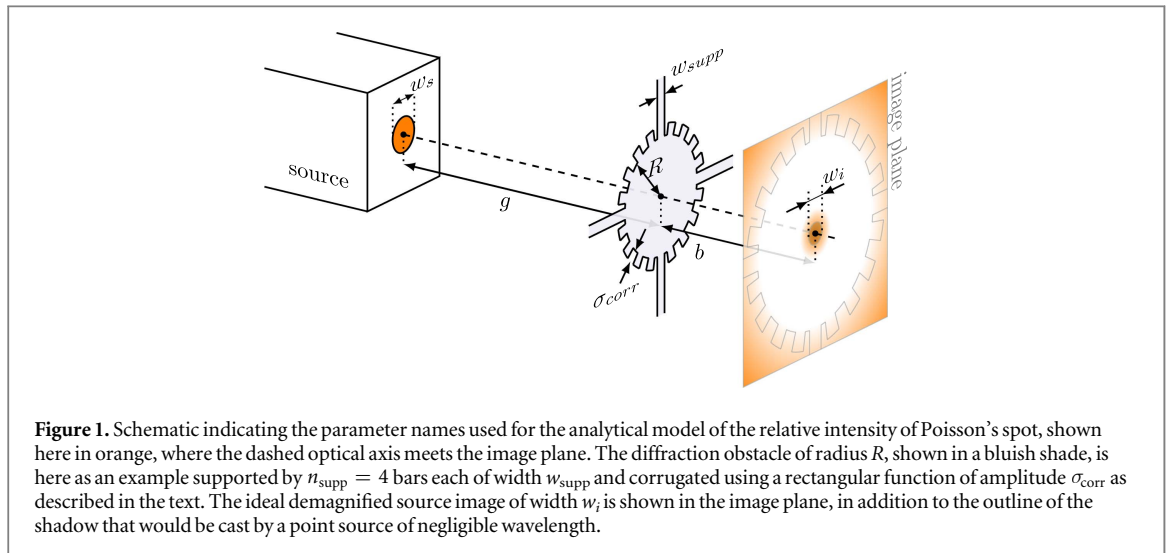
**1. Introduction**

One of the most tell-tale properties of waves in general is diffraction: the deviation from rectilinear propagation in the presence of obstacles due to interference [1]. In the history of science the phenomenon has helped to reveal the wave-character of light [2] and material particles such as electrons [3, 4], helium atoms and hydrogen molecules [5], and more recently  $C_{60}$  molecules [6] as well as large bio-molecules [7] exceeding 10 000 amu in mass. These latest diffraction experiments have sparked renewed interest in the particle-wave duality and the role of quantum decoherence [8] in the quantum-to-macroscopic world transition [9–11].

Diffraction in the Fresnel-regime, as the Talbot–Lau interferometers used in [7] belong to, is particularly useful in the determination of wave-nature, due to the possibility to observe diffraction from obstacles that are much larger than the wavelength of the incident wave. A most prominent effect in the Fresnel diffraction regime is Poisson's spot, also sometimes referred to as spot of Arago. It refers to the bright interference spot that can be observed in the shadow of an object with a circular rim such as a circular disc or sphere [12] (for brevity we call it a disc from here). Its prediction by SD Poisson and subsequent surprising observation by DFJ Arago established the wave-nature of light at the beginning of the 19th century. The intensity of Poisson's spot as a function of experimental parameters is the subject of this article.

As stated in many textbooks [13], for an ideal point source at infinity (plane wave) the on-axis intensity of Poisson's spot is equal to that of the undisturbed wave front (at equal distance from the source). This is referred to as unit relative intensity  $I_{\text{rel}} = 1$  in this article. Closer to the obstacle the ideal relative intensity is  $I_{\text{rel}} = \frac{b^2}{b^2 + R^2}$ , where  $R$  is the radius of the disc and  $b$  is the distance between disc and detector (see figure 1) [12].

In practice the intensity of Poisson's spot is affected by a number of experimental factors. These include beside the distances  $g$  and  $b$ , the source size, the diameter of the disc, any additional blocking due to support



structure and edge corrugation of the disc. Why the last of these parameters influences the spot intensity can be best understood using the Fresnel zone concept. The spot intensity results from the annular Fresnel zone adjacent to the rim of the disc [1]. The radial phase profile of the wave passing through this zone depends on the radius of the rim. A variation of the radius of the order of the width of the adjacent Fresnel zone thus results in destructive interference [14]. Finally, all the aforementioned factors must be considered in relation to the wavelength of the waves under consideration. Their effect will be discussed in detail in this article.

In the case of matter-waves, phase shifts may be incurred from interactions such as with the electromagnetic field, which also affect the intensity of Poisson's spot. For example, the application of an electric field in a wire-interferometer reduces the fringe period in the observed interference pattern [15]. Furthermore, the quantum-mechanical phase of neutral matter-waves is also affected in the vicinity of uncharged diffraction obstacles. This is due to the minute quantum-mechanical fluctuation of electric dipoles and the resulting attractive Casimir–Polder potential. These contributions to the intensity of Poisson's spot are beyond the scope of this article. The effect of the Casimir–Polder potential was covered in detail for matter waves by Nimmrichter *et al* [16, 17] and in one of our previous works [14]. A Poisson spot experiment realized for matter-waves utilizing a supersonic-expansion beam composed of deuterium molecules [18] did not show any noticeable effect in this respect, but is expected to become important in the case of more polarizable beam species like for example  $C_{60}$  molecules and even indium atoms [19]. The Poisson spot therefore can be used to measure interaction potentials of this kind.

Any ellipticity or an equivalent rotation of the disc are neglected in the model presented here. They both result in a lateral shape of the Poisson spot corresponding to the evolute of the elliptical diffracting rim, as was found by Coulson and Becknel [20, 21].

In addition to the already indicated applications, namely the study of the wave-particle duality for objects of increasing size and the measurement of particle–surface interaction potentials, a number of further applications have been suggested in the literature. For example, the characterization of wave-front aberrations in annular high-energy-laser systems using the transverse intensity distribution of Poisson's spot was proposed by Harvey and Forgham [22]. Also among them is the characterization of surface corrugation and shape of balls, as used for example in ball-bearings. In particular, Kouznetsov and Lara [23] proposed the use of the distance at which the Poisson spot vanishes behind the obstacle as a measure for its surface corrugation. The model we propose here improves upon this result by describing the decay of the Poisson spot as a function of distance behind the obstacle with the corrugation as the only free parameter. The extinction of Poisson's spot is also of relevance in the search for extra-solar planets, where a petal-shaped star shade has been proposed as part of an external coronagraph aiming at their detection and spectroscopic characterization [24]. Other applications include the precise and rapid measurement of the position of inertial fusion energy targets [25] and particle velocities in fluids [26]. Furthermore, the Poisson spot has been used in lithography to fabricate microtube arrays [27, 28], for which its shaping via incomplete spiral phase modulation [29] has interesting prospects.

This article is structured into four main sections. In the first one we present the analytical model as well as its derivation and limitations. In the second we describe the numerical simulation used to calculate the diffraction images in the detection plane and how we derived from them the relative intensity of Poisson's spot. In the third section, the light diffraction experiment, which we used to further validate the analytical model is reported on. Finally, the results from the analytical model, the numerical simulation and the experiment are compared in a separate results section. All is followed by a discussion and a conclusion.

## 2. Analytical model

In this section we derive an analytical formula valid in the Fresnel regime for the relative peak intensity of Poisson's spot in the presence of finite spatial coherence and imperfections of the diffraction obstacle. The starting point for the analytical model is the lateral intensity distribution of Poisson's spot from a source of plane waves (point source at infinite distance) in the Fresnel regime, which can be expressed in terms of a zero-order Bessel function of the first kind  $J_0$  [22]:

$$I_{\text{pw}}(r) = \frac{b^2}{b^2 + R^2} J_0^2\left(\frac{r}{w_p/2}\right) = \frac{b^2}{b^2 + R^2} J_0^2\left(r \frac{2R\pi}{\lambda b}\right) \approx J_0^2\left(r \frac{2R\pi}{\lambda b}\right). \quad (1)$$

Here,  $r = \sqrt{x^2 + y^2}$  is the radial lateral coordinate in the detection plane.  $r$  is assumed to be small.  $w_p$  is the full-width at half-maximum (FWHM) of the plane-wave Poisson spot. The latter can be expressed in terms of the radius of the disc  $R$ , the wavelength  $\lambda$  at which the source emits, and the length  $b$ , which is the distance from diffraction obstacle to detection plane as mentioned before. The Fresnel approximation requires that  $\lambda \ll R$  and  $b \gg R$ . The fraction in front of the Bessel function is thus very close to  $\frac{b^2}{b^2 + R^2} \approx 1$  and we will neglect it therefore from here on. Note that we assumed incoming plane waves in this first step and thus the source distance  $g$  to be infinite. We therefore do expect deviations from our model for small values of  $g$ .

The influence of the partial spatial coherence of the source, i.e. the source width, results in a much more significant variation of the relative on-axis intensity. The derivation of an analytical model that reflects this variation (see equation (2)), and thus gives the correct dependence on  $g$  ( $g$  larger than a few disc radii), is presented in the following paragraphs. In brief, we first note that off-axis source points result in 2d point-spread function images equal to the plane wave Poisson spot given in equation (1), but with an offset from the optical axis. The extended-source Poisson spot corresponds to an incoherent super-position of these point-spread function images, which we express using a 2d convolution integral. For on-axis points the integral has an exact solution.

First the lateral offset of the off-axis point-source Poisson-spot images in the detection plane can be explained as follows. The point-source Poisson spot images will be at the exact center of the shadow cast by each off-axis point-source. It is therefore located at the intersection point of the detection plane and the line going through source point and disc center, giving the magnification factor  $\frac{b}{g}$ . The extended-source Poisson spot therefore results in a magnified or de-magnified image of the source depending on the value of this factor (see also [12]).

The lateral intensity distribution  $I_{\text{xs}}(r)$  of Poisson's spot from a source of diameter  $w_s$  is then given by a convolution of  $I_{\text{pw}}(r)$  with the function  $I_i(r)$  defined below. The latter represents the ideal image of the source that would be formed by a delta-function as point-spread-function. We assume that the source emits evenly from a circular area of diameter  $w_s$  and take into account that the self-image formed in the detection plane is magnified by the factor  $\frac{b}{g}$  as explained above and would be also the case for a thin lens in geometrical optics:

$$I_i(r) = \begin{cases} \frac{1}{\pi(w_i/2)^2} & \text{if } |r| < w_i/2, \\ 0 & \text{elsewhere,} \end{cases}$$

where  $w_i = w_s \frac{b}{g}$  is the FWHM of the ideal source image. The Poisson spot  $I_{\text{xs}}(r)$  from a spatially incoherent source is thus characterized by the following convolution integral in polar coordinates:

$$I_{\text{xs}}(r) = I_{\text{pw}}(r) * I_i(r) = \int_0^{2\pi} \int_0^\infty J_0^2\left(\frac{r-t}{w_p/2}\right) I_i(t) t \, d\phi dt.$$

We are interested in the peak intensity at  $r = 0$  and can therefore evaluate the integral as follows [30]:

$$\begin{aligned} I_{\text{rel, xs}} &= I_{\text{xs}}(0) = \int_0^{2\pi} d\phi \int_0^{w_i/2} J_0^2\left(-\frac{2t}{w_p}\right) \frac{4}{\pi w_i^2} t \, dt \\ &= J_0^2\left(\frac{w_i}{w_p}\right) + J_1^2\left(\frac{w_i}{w_p}\right) \\ &= J_0^2\left(\frac{w_s R \pi}{g \lambda}\right) + J_1^2\left(\frac{w_s R \pi}{g \lambda}\right). \end{aligned} \quad (2)$$

This surprisingly simple equation forms the centerpiece of the analytical model and shows that  $I_{\text{rel, xs}}$  is independent of  $b$  for an extended uniform source and ideal spherical obstacle. For other axially symmetric shapes, such as that of rectangular obstacles, which also result in an on-axis intensity enhancement, a numerical

approach as described in section 3 must be used. The Bessel-functions in equation (2) can be evaluated directly in most mathematics software packages to arbitrary precision, but for completeness we note the following asymptotic form for large ratios  $\frac{w_i}{w_p}$  [30]:

$$I_{\text{rel},xs} \approx \frac{2 w_p}{\pi w_i} = \frac{2}{\pi^2} \frac{g \lambda}{w_s R}. \quad (3)$$

If we define the transverse coherence length  $l_c$  of the source of diameter  $w_s$  at a distance  $g$ , in the usual way, namely by  $l_c = \frac{\lambda g}{2w_s}$ , it is clear that the intensity of Poisson's spot is directly related to the degree of coherent illumination of the disc:

$$I_{\text{rel},xs} \approx \frac{4}{\pi^2} \frac{l_c}{R}. \quad (4)$$

Thus, to observe the intensity of Poisson's spot to be as large as if the disc was not there, i.e.  $I_{\text{rel},xs} \approx 1$ , one can as a rule of thumb state that the transverse coherence of the beam incident on the disc must be approximately equal to the diameter of the disc.

Furthermore, it should be noted that if the source width exceeds the radius of the disc, i.e.  $w_s > R$ , the geometric width of Poisson's spot  $w_i$  may become larger than the geometrical shadow (umbra shadow) width  $w_u = 2R + \frac{b}{g}(2R - w_s)$ , making the observation of Poisson's spot increasingly difficult. To ensure that  $w_i < w_u$  we must have

$$\frac{b}{g} < \frac{R}{w_s - R} \quad \text{if } w_s > R. \quad (5)$$

For large wavelengths the width of Poisson's spot will be even larger and the shadow even narrower than assumed for this purely geometrical requirement, restricting its visibility to even smaller  $b/g$ .

Beside partial spatial coherence a deviation of the shape of the diffraction obstacle from a circular cross-section reduces the relative intensity of Poisson's spot. The experimental parameter we consider in this respect is the edge corrugation of the disc. Its effect on the on-axis diffraction intensity can be best understood by considering the vibration curve [1] depicted in figure 2. It is a visual representation of the Fresnel–Kirchhoff integral shown in equation (8) below. The resulting phasor  $A(P)$  (point  $P$  on the optical axis) is composed of the infinitesimal phasors, each corresponding to a particular radius in the integration plane, that when joined head-to-tail follow the vibration curve. The end of the spiral is located at point  $Z_\infty$ , resulting in the expected unit amplitude of  $A(P)$ , if none of the incident field is blocked. However, if part of the integration plane is blocked by a disc with origin at the optical axis, the resulting phasor starts at the point on the vibration curve that corresponds to the radius of the rim of the disc, instead of the point  $Z_0$ .

The edge corrugation can be thus accounted for by an averaging of the phasors that correspond to the different disc radii. A rotation of the phasor by  $\theta = 180^\circ$  corresponds to a change in the radius by one Fresnel zone, which results in a near complete cancellation of the amplitude or intensity of Poisson's spot if the two phasors are averaged. The width of a Fresnel zone starting from a particular radius  $R$  is approximately given by  $w_{fz} = \sqrt{R^2 + \frac{\lambda g b}{(g+b)}} - R$ . We assume from here that the corrugation is less than the width of the adjacent Fresnel zone, and that the intensity is negligible for corrugation of larger amplitude. The latter is not accurate for ideally shaped rectangular corrugation profiles, but we are more interested in finding a worst-case analysis for random edge corrugation. Neglecting the change in length of the phasors due to the spiral shape of the vibration curve, the averaging of the phasors can be accomplished by averaging the projections of the phasors in the direction of the resulting phasor.

The special case of a square wave corrugation profile with a peak-to-peak amplitude  $\sigma_{\text{corr}} = R_{\text{max}} - R_{\text{min}}$  and sufficiently small period is depicted in figure 2. The phasors  $A_{\text{min}}$  and  $A_{\text{max}}$  correspond to the part of the corrugated edge with radii  $R_{\text{min}}$  and  $R_{\text{max}}$ , respectively. As long as  $\sigma_{\text{corr}} < w_{fz}$ , the resulting phasor  $A_{\text{corr}}$  is then rotated half-way between the two and its length is thus given by  $|A_{\text{min}}| \cos(\theta/2) \approx |A_{\text{max}}| \cos(\theta/2)$ . A rotation of the phasor by  $\theta = \pi$  corresponds to a change in the radius by  $w_{fz}$ . For simplicity we assume that the phase angle of the phasors is approximately proportional to  $R$  (more precisely we have that phase  $\propto R^2$ ), and we can thus write

$$|A_{\text{corr}}| \approx |A_{\text{min}}| \cdot \cos\left(\frac{\pi \sigma_{\text{corr}}}{2 w_{fz}}\right).$$

Since the measured intensity at point  $P$  corresponds to the square of the length of the resulting phasor, the attenuation due to rectangular-profile corrugation can be accounted for by the following factor (with attenuation we here refer to the ratio between the on-axis intensity behind a corrugated disc and the on-axis intensity behind a disc of perfect circular shape):

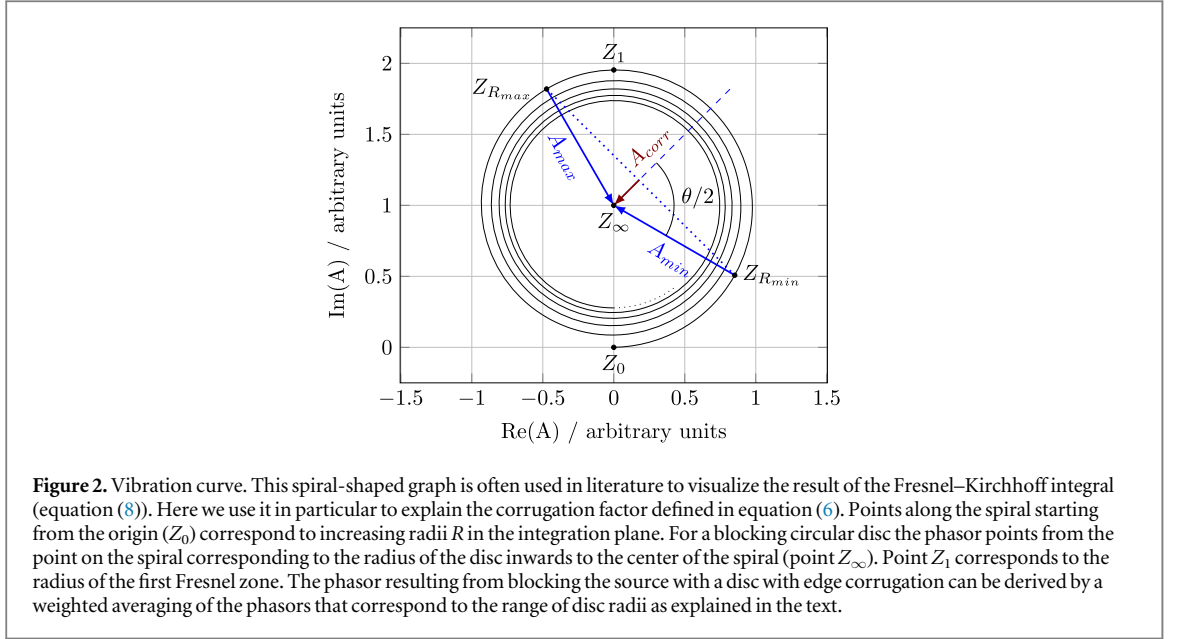


**Figure 2.** Vibration curve. This spiral-shaped graph is often used in literature to visualize the result of the Fresnel–Kirchhoff integral (equation (8)). Here we use it in particular to explain the corrugation factor defined in equation (6). Points along the spiral starting from the origin ( $Z_0$ ) correspond to increasing radii  $R$  in the integration plane. For a blocking circular disc the phasor points from the point on the spiral corresponding to the radius of the disc inwards to the center of the spiral (point  $Z_\infty$ ). Point  $Z_1$  corresponds to the radius of the first Fresnel zone. The phasor resulting from blocking the source with a disc with edge corrugation can be derived by a weighted averaging of the phasors that correspond to the range of disc radii as explained in the text.

$$C_{\text{corr}} = \begin{cases} \cos^2\left(\frac{\pi}{2} \frac{\sigma_{\text{corr}}}{w_{\text{fz}}}\right) & \text{if } \sigma_{\text{corr}} < w_{\text{fz}}, \\ \sim 0 & \text{otherwise.} \end{cases} \quad (6)$$

Finally, we take into account that in most realizations of the Poisson spot experiment the disc needs to be fixed in space by some type of support structure. In the model we propose, we assume the use of a number  $n_{\text{supp}}$  of straight radial support bars each of width  $w_{\text{supp}}$ . Together they block a distance  $n_{\text{supp}} \cdot w_{\text{supp}}$  along the circumference of the disc. Again we use the vibration curve and the concept of phasor averaging to derive the effect on the on-axis intensity. If we set the phasors corresponding to blocked parts of the disc's circumference to zero, then it is clear that the attenuation is proportional to the ratio of unblocked circumference to the total circumference. We thus include the following factor  $C_{\text{supp}}$  in the model with a proportionality constant  $c_{\text{supp}}$ .

$$C_{\text{supp}} = 1 - \frac{c_{\text{supp}} n_{\text{supp}} w_{\text{supp}}}{2 \pi R}.$$

We do expect a certain dependence of  $c_{\text{supp}}$  on the Fresnel number of the particular setup since the Fresnel zones at larger radii are blocked at decreasing proportions (see section 5.4).

The complete analytical model for the relative on-axis intensity of Poisson's spot is thus given by:

$$I_{\text{rel,model}}(g, b, \lambda, w_s, R, \sigma_{\text{corr}}, w_{\text{supp}}, n_{\text{supp}}) = I_{\text{rel,xs}} \cdot C_{\text{corr}} \cdot C_{\text{supp}}. \quad (7)$$

The equation can be evaluated at a small fraction of the computational expense of the numerical simulations described below. Its validity is going to be tested in the following two sections.

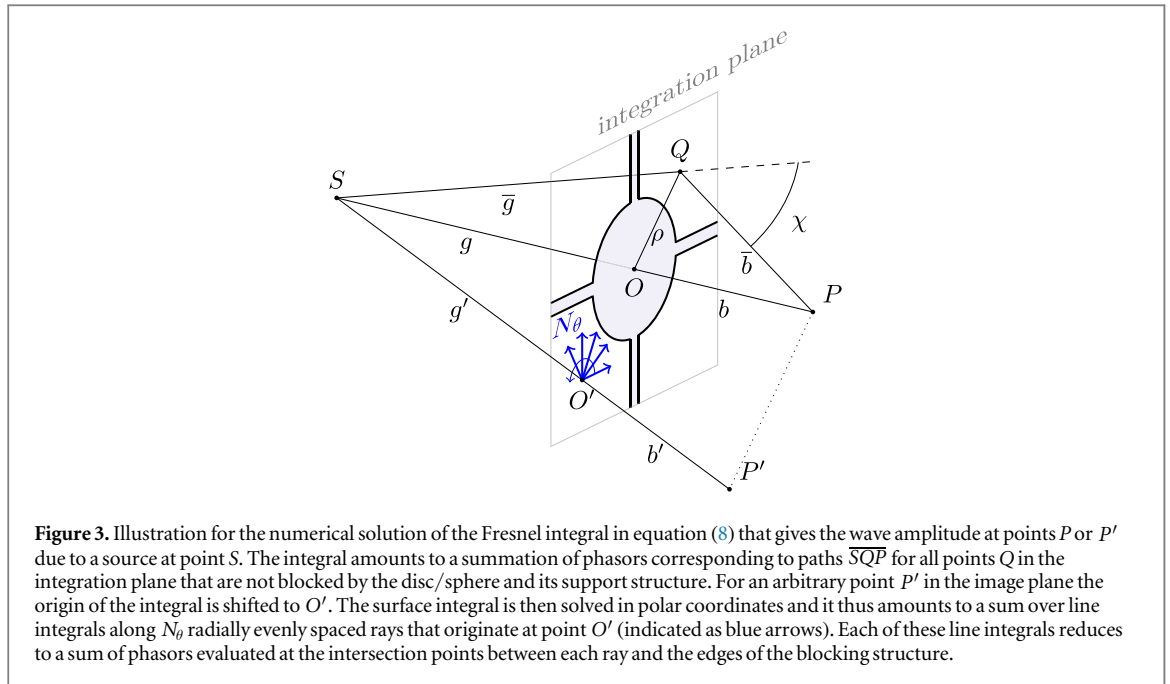
### 3. Numerical methods

The intensity of Poisson's spot can be calculated directly by a numerical evaluation of the Fresnel–Kirchhoff diffraction integral, which can be used to express the amplitude and phase at a point  $P$  in the following way:

$$A(P) = -\frac{i}{\lambda g b} \int_0^{2\pi} \int_0^\infty g(\rho, \theta) e^{\frac{i\pi\rho^2}{\lambda} \left(\frac{1}{g} + \frac{1}{b}\right)} \rho \, d\rho \, d\theta. \quad (8)$$

Here,  $\rho$  and  $\theta$  are the polar coordinates in the integration plane as indicated in figure (3). The binary function  $g(\rho, \theta)$  evaluates to zero for blocked parts of the integration plane and to one for transparent regions. The formulation makes use of the Fresnel approximation, which implies that the inclination factor  $\frac{1}{2}(1 + \cos(\chi))$  was neglected and the path lengths used to calculate the phase only take into account up to square terms in the Taylor expansions of  $\bar{g} = \sqrt{g^2 + \rho^2}$  and  $\bar{b} = \sqrt{b^2 + \rho^2}$ . Furthermore, we assume that for the calculation of arbitrary points  $P'$  in the image plane  $g = g'$  and  $b = b'$ . These are good approximations as long as  $\chi$  is small, which corresponds to the parameter space we are interested in here.

The surface integral is solved numerically following the approach discussed in [31] and summarized in figure (3). A more efficient and stable numerical solution was found by Nimmrichter [16] for the special case of perfectly round discs that uses Wigner functions and Babinet's principle, but is not easily adapted to discs with



support structure and/or corrugation. A direct approach to solving the surface integral, for example by summing phasors corresponding to all points  $Q$  in the integration plane turns out to be numerically unstable. In the numerical simulation presented here, for each point  $P'$  in the point-source diffraction image we sum over  $N_\theta = 19997$  line integrals along rays that simplify to a sum over as many terms as there are intersection points of the ray with the disc or support structure. The number  $N_\theta$  was chosen to be a prime number in order to avoid artificial fringes from symmetry in the numerical evaluation. The number results in a minimal resolution of about  $0.3 \mu\text{m}$  across an integration plane of about 1 mm width. This is enough to resolve the minimal Fresnel zone widths in the simulated experiments of a few micrometer. Unlike in [31], we find the intersection points of the rays (shown in blue) with the edges of the blocking structure (disc/sphere and support bars) analytically and not using the search algorithm proposed there. We implemented the algorithm in the C programming language and the required computation time for its execution ranged from 140 to 250 minutes per complete diffraction image (using a single core of a two-CPU Quadcore AMD Opteron 2376 system equipped with 64 GB RAM).

The edge corrugation ( $\sigma_{\text{corr}}$ ) was not taken into account in these calculations, to allow for acceptable computation times. We studied the effect, however, in the experiments described in the next section. To account for the size of the source each computed point-source diffraction image is convoluted with the demagnified image of the source of width  $w_i$  using a Matlab program. The outer aperture was assumed to be of infinite radius in the simulation, while in the experiments it was 5 mm. Its proper inclusion would unnecessarily increase the minimal resolution required in the diffraction images, as the additional oscillations it introduces to the point source diffraction images are washed out after convolution with the source image. Support structure bars of varying number and width were taken into account in the calculations. Therefore, the calculation of the point-source diffraction image could not be simplified by only calculating  $A$  for points  $P'$  along a radial line, with the full image deducible from axial symmetry. The computed images for supported discs thus covered one half of the full image plane and were composed of 1001 by 501 pixels. Before the source image convolution the remaining half-image could be deduced from mirror symmetry since we suitably arranged the simulated support bars.

#### 4. Experimental methods

In order to find any possible errors of the analytical model and the simulation described above, we measured the relative intensity of Poisson's spot with the setup shown schematically in figure 4. It was realized using components from Thorlab's 30 mm cage system. Three light emitting devices (LED) of type CREE XP-E2 and colors red (XPE-BRD-L1-0000-00801 specified dominant wavelength (DWL) range  $(625 \pm 5) \text{ nm}$ ), green (XPE-BGR-L1-0000-00F01 DWL =  $(527.5 \pm 7.5) \text{ nm}$ ), and blue (XPE-BBL-L1-0000-00301 DWL =  $(475 \pm 10) \text{ nm}$ ) emitted light into a viewing angle of about  $130^\circ$ . An aspherical lens (Thorlabs C671TMEA,  $f = 4.02 \text{ mm}$ ) then focused the divergent beam of light onto a ground glass screen. Adjacent to the ground side of this glass slide (which was facing away from the LED) we attached a thin metal sheet with a round

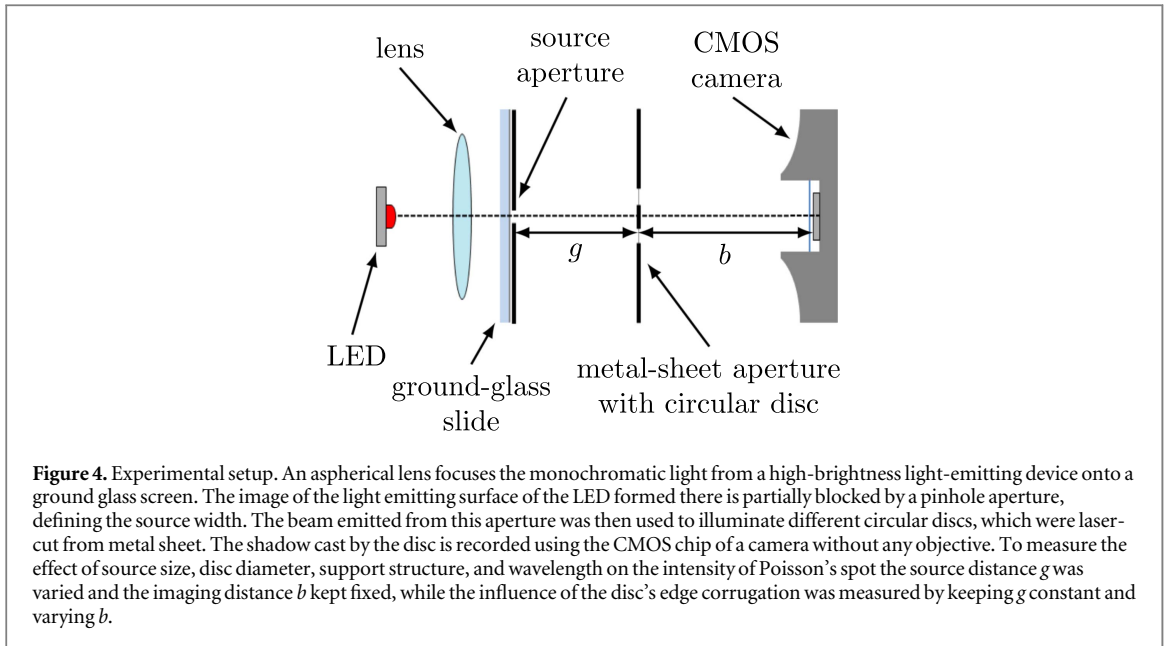


**Table 1.** Parameters of the stainless steel pinhole apertures (named 'source aperture' in figure 4) used in the experiment. The given errors are mainly due to deviations from circularity.

Aperture ID	Diameter $w_s$ ( $\mu\text{m}$ )	Absolute error $\Delta w_s$ ( $\mu\text{m}$ )
50	55.7	5.4
100	104.1	5.5
200	208.8	5.4

pinhole aperture of different diameters (see table 1 and supplementary information for microscopy images is available online at [stacks.iop.org/NJP/19/033022/mmedia](https://stacks.iop.org/NJP/19/033022/mmedia)). The spatial coherence of the light emitted from the pinhole is thus determined by the pinhole's dimension, as long as the image of the LED source projected onto the ground glass screen is larger than the pinhole, which was the case for our experiments. In order to block light not passing through the pinhole the components were mounted in a single Thorlabs cage plate and remaining stray-light blocked with black Plasticine-type modeling clay. Laboratory background-light was suppressed with a cardboard encapsulation. Reflections from cage components and other surfaces was reduced by painting them with black permanent marker as well as a varying amount of apertures made from black cardboard.

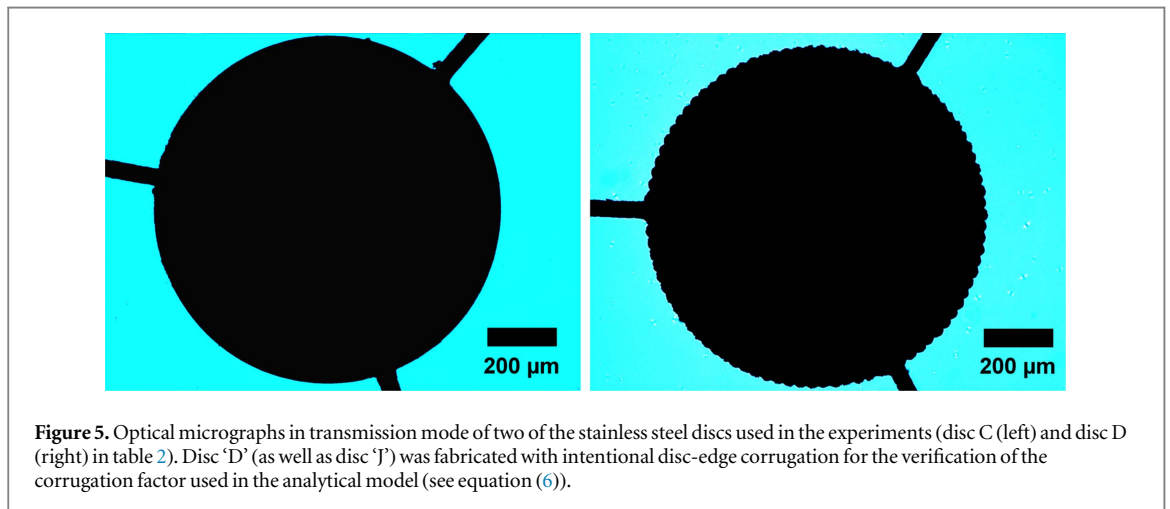
The thus spatially filtered light was incident onto a series of different discs varying in disc diameter, disc-edge corrugation and supporting structure. The discs were laser-cut in-house from thin (0.05 mm thickness) sheets of stainless steel using a picosecond laser. The discs were supported by two to four support bars inside 5 mm diameter pinholes (see table 2, figure 5 and supplementary information for a complete collection of microscopy images [stacks.iop.org/NJP/19/033022/mmedia](https://stacks.iop.org/NJP/19/033022/mmedia)).

The shadow intensities within the shadow cast by each disc was recorded without imaging optics using a monochrome USB CMOS camera (Thorlabs DCC1545M). The camera's sensor chip consisted of an array of 1280-by-1024 pixels each approximately 5.2  $\mu\text{m}$  in width. It thus provides an imaging area (6.6 mm by 5.5 mm) large enough to capture the light directly incident from the source and at the same time high enough resolution to image Poisson's spot at the center of the disc's shadow. The higher sensitivity provided by EMCCD or sCMOS chips would allow for higher precision measurements in the future. Here a custom-programmed National Instruments Labview Virtual Instrument was used to capture and average image-data for sufficient sensitivity. For each recorded image, first the exposure time and master gain (the latter only for the longer source-to-detector distances) were adjusted such that the undisturbed intensity corresponded to about 70% of the full-intensity level. To reduce noise, 100 frames were accumulated and averaged for each setting. Furthermore, for each of these averaged images, a background image recorded with a black-cardboard shutter in place, using equal exposure time and averaging, was subtracted. The shutter was located approximately half-way between source and disc, to be able to account for as much stray light from the source as possible.

Each recorded diffraction image was analyzed using a Matlab script in the following way. First we determined a rough center location of the disc's shadow in each image by finding the minimum of a suitably

**Table 2.** Parameters of the stainless steel discs used in the experiment.

Disc ID	Radius $R$ ( $\mu\text{m}$ )	$\sigma_{\text{corr}}$ ( $\mu\text{m}$ )	$w_{\text{supp}}$ ( $\mu\text{m}$ )	$n_{\text{supp}}$
A	496.1	1.68	198.1	2
B	495.8	1.91	27.8	3
C	496.8	2.54	52.5	3
D	486.3	4.95	49.3	3
E	494.1	2.52	102.3	3
F	495.9	1.94	199.1	3
G	495.9	1.48	197.5	4
H	146.4	1.80	47.9	3
I	246.7	1.74	48.7	3
J	256.3	5.94	46.0	3



convoluted version of the same image. The precise center location of the Poisson spot in each image was computed by fitting a two-dimensional error-function-based model to the spot (see figures 3-18 in supplementary information). The Poisson spot intensity  $I_{\text{PS}}$  was then taken as the intensity recorded by the pixel of the CMOS camera closest to this center location (see columns ‘ $I_{\text{PS}}$  mark’ of tables 3-18 in supplementary information for pixel location of each image).

Next we determined the unobstructed intensity  $I_0$  in the detection plane, which we need to calculate the relative intensity  $I_{\text{rel}} = I_{\text{PS}}/I_0$ . To measure the unobstructed intensity for each data point we masked any regions in the recorded images that contained shadows or intensity oscillations due to diffraction (see columns ‘ $I_0$  mask’ of tables 3-18 in supplementary information). The unobstructed intensity we recorded as the average value of the unmasked image pixels. The uncertainty of  $I_0$  we estimate to be plus and minus one standard deviation of the intensities of the unmasked pixels. For the uncertainty of  $I_{\text{PS}}$  we assume the same relative uncertainty as that of  $I_0$ . In the data sets used to determine the effect of corrugation and wavelength we have additionally removed varying background intensity by subtracting the minimum intensity value within the shadow region from both  $I_{\text{PS}}$  and  $I_0$ .

Fixed distances between pinhole and free-standing disc (object distance  $g$ ) as well as between free-standing disc and CMOS chip (image distance  $b$ ) were measured with a hand-held caliper (Hommel, 0.05 mm reading precision), while the variable one of the two distances was measured and set with an attached digital caliper (Mitutoyo Absolute 572-211-20, 0.01 mm reading precision, 0.03 mm accuracy).

The dimensions of the free-standing disc samples as well as of the pinhole aperture used to restrict the source size were determined from optical microscopy images. The distances between pixels in the microscopy images were determined using a calibration scale (Keyence OP-51491). Accurate values for the diameter and edge corrugation of the discs we derived from the microscopy images using a Matlab script. The script first detects the edge of the disc using a 2d-convolution based algorithm and then finds the center pixel by minimizing the standard deviation of distances to the disc edge. The mean of the distances of the edge from this pixel less one standard deviation is taken as the radius of the disc  $R$  and the disc’s edge corrugation  $\sigma_{\text{corr}}$  as twice the standard deviation of those distances.

**Table 3.** Overview table of the performed diffraction experiments. The uncertainty in  $g$  and  $b$  is about 0.5 mm. Column ‘Figure’ is used to indicate the graphs where the data sets are displayed. Column ‘ $F$ ’ gives the corresponding Fresnel number range ( $F = \frac{R^2}{\lambda} \frac{g+b}{gb}$ , which corresponds to the number of Fresnel zones blocked by the disc).

#	Figure	$\lambda$ (nm)	Aperture	Disc	$g$ (mm)	$b$ (mm)	$F$
1	6	$625 \pm 5$	‘50’	B	15.9–125.9	29.5	38–17
2	6, 8, 9	$625 \pm 5$	‘100’	B	15.9–125.9	29.5	38–17
3	6	$625 \pm 5$	‘200’	B	15.9–125.9	29.5	38–17
4	7	$625 \pm 5$	‘100’	C	15.9–125.9	29.5	38–17
5	7	$625 \pm 5$	‘100’	I	15.9–125.9	29.5	9–4
6	7, 9	$625 \pm 5$	‘100’	H	15.9–125.9	29.5	3–1
7	8	$527.5 \pm 7.5$	‘100’	B	15.9–125.9	29.5	45–20
8	8	$475 \pm 10$	‘100’	B	15.9–125.9	29.5	50–22
9	9	$625 \pm 5$	‘100’	A	15.9–125.9	29.5	38–17
10	9	$625 \pm 5$	‘100’	E	15.9–125.9	29.5	38–16
11	9	$625 \pm 5$	‘100’	F	20.9–125.9	29.5	32–17
12	9	$625 \pm 5$	‘100’	G	15.9–125.9	29.5	38–17
13	11	$475 \pm 10$	‘100’	I	60.6	4.6–46.6	30–5
14	11	$475 \pm 10$	‘100’	J	60.6	4.6–46.6	32–5
15	11	$475 \pm 10$	‘100’	C	60.6	2.8–64.8	194–20
16	11	$475 \pm 10$	‘100’	D	60.6	4.6–66.6	186–19

## 5. Results

We have measured the relative intensity of Poisson’s spot for different experimental parameters and compare the resulting data series with both the proposed analytical and numerical models in the following subsections.

### 5.1. Source width

In the data sets shown in figure 6 we explored the dependence of  $I_{\text{rel}}$  on the diameter of the approximately circular source pinhole aperture. For this purpose the apertures whose different diameters are noted in table 1 were used. For each aperture  $I_{\text{rel}}$  was measured as described in the previous section as a function of the source distance  $g$ . Both analytical and numerical model fit well to the measured data with some exceptions. These are discussed in the following paragraphs.

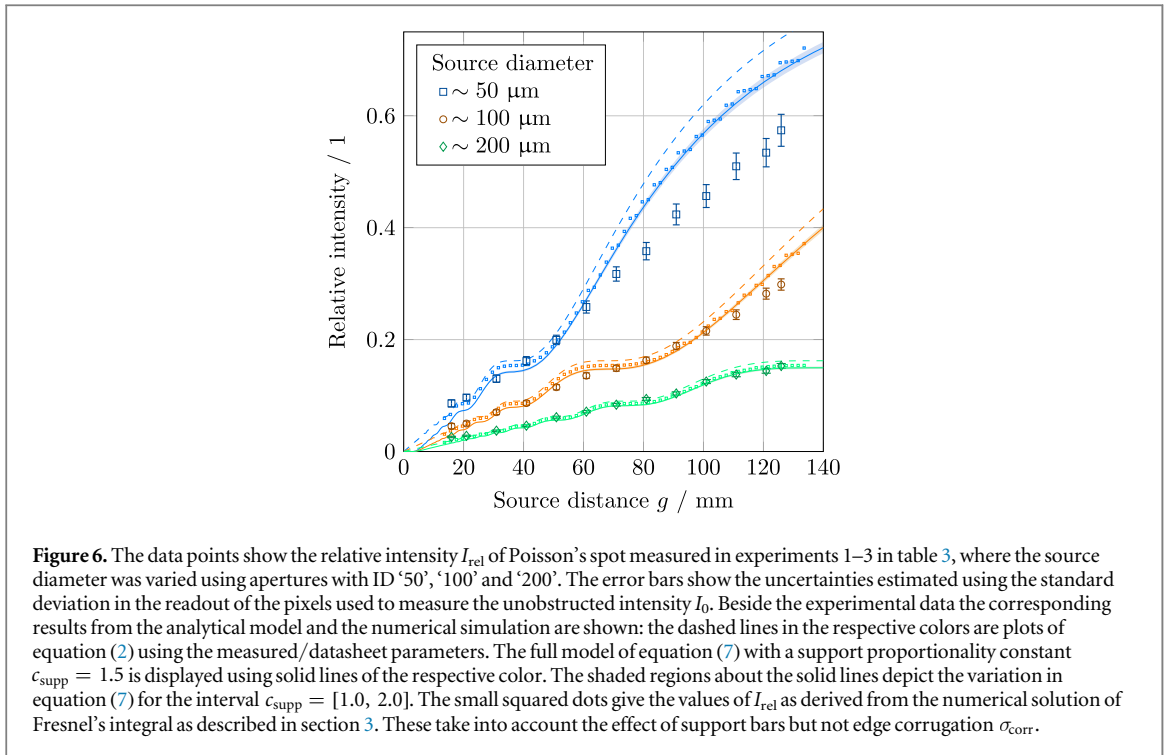
At large distances  $g$  especially the small source data set starts to deviate to lower intensities than predicted by the models. This occurs when the Poisson spot is of similar or smaller width than the pixel width of the camera. The pixel readout is then expected to be lower, since only part of the pixel area is lit with the full peak on-axis intensity to be measured. For example, for the dataset corresponding to pinhole ‘50’ at a distance of  $g = 126$  mm the expected image width is  $w_i = 11.7 \mu\text{m}$  and the FWHM of the point source Poisson spot is  $w_p = 5.9 \mu\text{m}$ , which are both only slightly larger than the pixel width of the camera of  $5.2 \mu\text{m}$ .

At distances  $g$  below about 20 mm an increase in the relative intensity can be seen in all three data sets. This we attribute to additional background signal from reflections inside the tubing when the source is at close approach to the CMOS camera. The subtracted background images could not fully remove this effect, since the central beam blocked by the shutter flag also contributes to reflections inside the black tubing between disc and camera. The latter effect is particularly strong for small source distances since the divergence of the beam, which is determined by the outer aperture of the disc sample, is largest there, and the collimated beam effectively lights a much larger area than the CMOS chip alone.

The simulation data points confirm the analytical model well. The only deviation between the two models occurs at small  $g$ , where the attenuating effect of edge corrugation starts to show in the analytical model. As mentioned above, the latter was not accounted for in the numerical simulation. For the smallest aperture at large  $g$  the numerical data points show steps, which are due to the limited lateral resolution of the simulated point-source diffraction images (about  $0.3 \mu\text{m}$  at  $g = 133.6$  mm).

### 5.2. Disc radius

In figure 7 we compare the relative intensity of Poisson’s spot for three different disc sizes. For the smallest disc diameter of 0.3 mm we find the best correspondence to the numerical model even at large distance  $g$ . The large value of the FWHM of the point-source Poisson spot expected for that data set ( $w_p = 39.1 \mu\text{m}$ ), ensures that the measurement is not limited by the resolution of the CMOS camera ( $5.2 \mu\text{m}$  pixel size) to the same extend as in the pinhole ‘50’ source width data set. The resolution of the numerical point-source diffraction image (which was scaled in the range of  $0.29$ – $0.09 \mu\text{m}$  according to the width of the geometric shadow) was sufficient as well.



As the de-magnification of the source image increases with  $g$  and the smaller value of  $w_p = 11.7 \mu\text{m}$  for the 1 mm disc data set, its deviation from the numerical data points is the most significant at large values for  $g$ .

A comparison between the graphs of the analytical and the numerical model shows that the assumed value of the constant  $c_{\text{supp}} = 1.5$  slightly underestimates the dampening effect of the three support bars. Note also that the experimental data at small  $g$  for the 1 mm disc better corresponds to the numerical simulation. This can be explained by an overestimate of the effect from surface corrugation in the analytical model, which could be in part due to the square-wave type shape of the corrugation assumed there. Another likely explanation is unaccounted for background due to the close vicinity of the source. As shown in section 5.5, the effect of corrugation is well described using the analytical model, especially if additional care is taken to remove background. Therefore we deem the latter explanation to be correct.

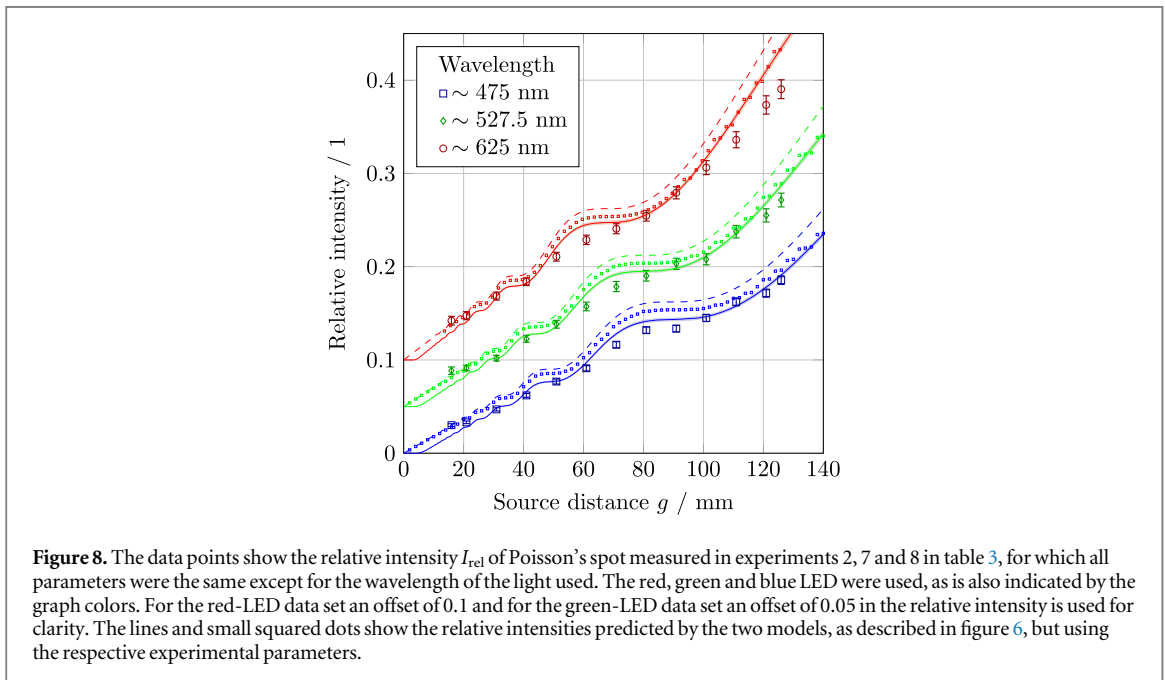
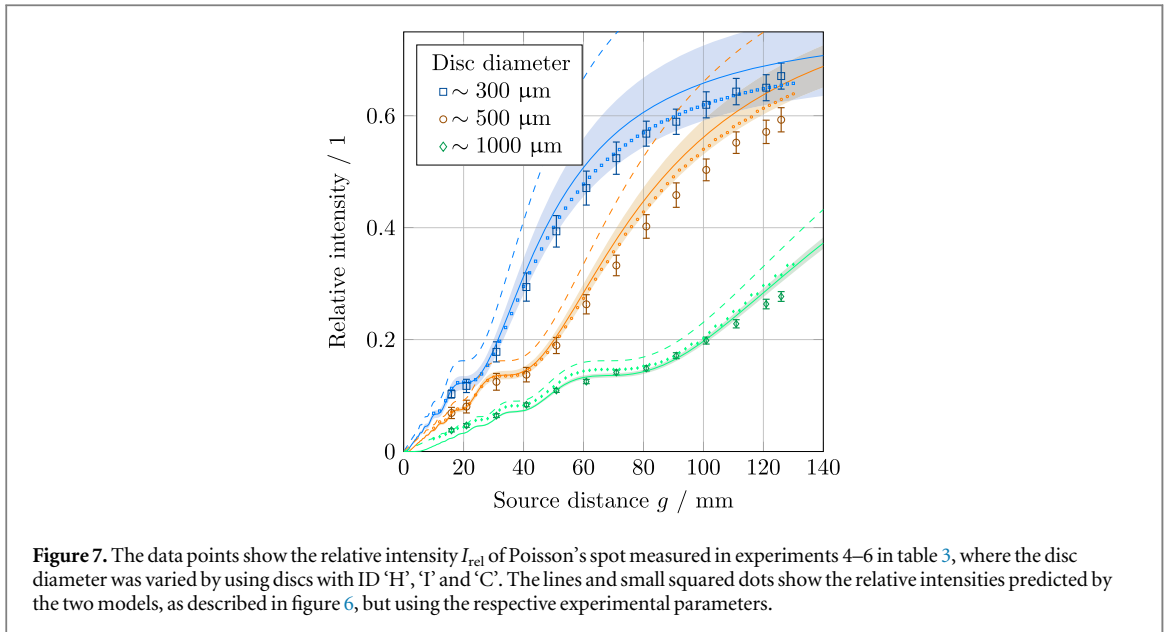
### 5.3. Wavelength

To good approximation the relative intensity of Poisson's spot is directly proportional to the wavelength (see equation (3)) if  $w_i/w_p$  is large. In figure 8 we compare experimental data recorded using three different source wavelengths and compare it to the numerical and analytical model. The correspondence is good in general. The relative intensity is expected to deviate from the approximate linear dependence on  $g$  in the form of oscillations. At the largest peak of these oscillations at about  $g = 60\text{--}80$  mm small reductions in the measured intensities compared to the models can be noted. This we attribute to the fact that these oscillations are associated with only part of the source image formed by Poisson's spot, and thus it would require a higher resolution detector to reproduce them in the experiment (see also figure 10).

The deviation between numerical and analytical model is more pronounced for the short wavelength data set. This is expected, since the disc edge corrugation, which is not accounted for in the numerical simulation, is most significant for the blue-LED light. The small deviation to larger intensity values at small  $g$  is equally visible in the three data sets and is most likely due to unaccounted for background as in the data sets discussed before.

### 5.4. Support structure

The effect of width and number of radial support bars on  $I_{\text{rel}}$  is examined in figure 9. The deviation of the experimental data from the dashed lines (equation (2)) increases for an increasing amount of blocked disc circumference, as expected. The analytical model explains the reduction in  $I_{\text{rel}}$  well as long as a variation in the proportionality constant  $c_{\text{supp}}$  in the interval  $[1.0, 2.0]$  is allowed. The camera resolution and background related deviations that also show in these data sets at the edges of the source distance range we have discussed already above. The two experimental data sets recorded with discs supported by an even number of support bars both show a trend toward higher intensities within the limits of the analytical model, but to the surprising extend that



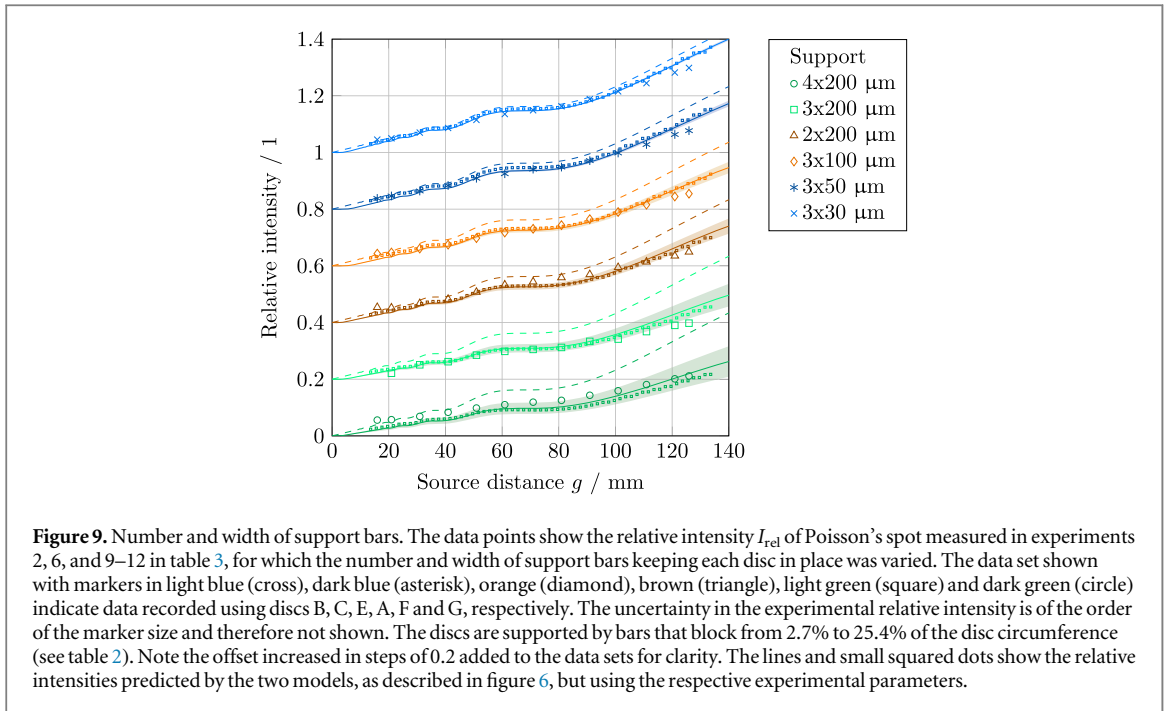
the relative intensities measured behind disc 'G' exceed those measured behind disc 'F'. The relative intensities measured behind disc 'A' exceed those behind disc 'E' up to approximately  $g = 100$  mm. However, since this trend is not reproduced by the numerical simulation we attribute this to a systematic error possibly caused by additional background.

The effect of the support structure on the shape of Poisson's spot can be seen in figure 10, where we compare two-dimensional images from both experiment and numerical simulation in an exemplary fashion. A complete set of two-dimensional diffraction images corresponding to the on-axis relative intensity data points in figures 6–9, 11 and 12 can be found in the supplementary information.

The sensitivity of the support structure measurements can be improved in the future by using smaller disc radii (see figure 7), which was not done here due to the increased difficulty in accurately fabricating the smaller free-standing discs.

### 5.5. Disc edge corrugation

The accuracy of the proposed factor accounting for the effect of disc edge corrugation on the relative intensity of Poisson's spot (equation (6)) we investigated in the data sets presented in figures 11 and 12. Note that in contrast



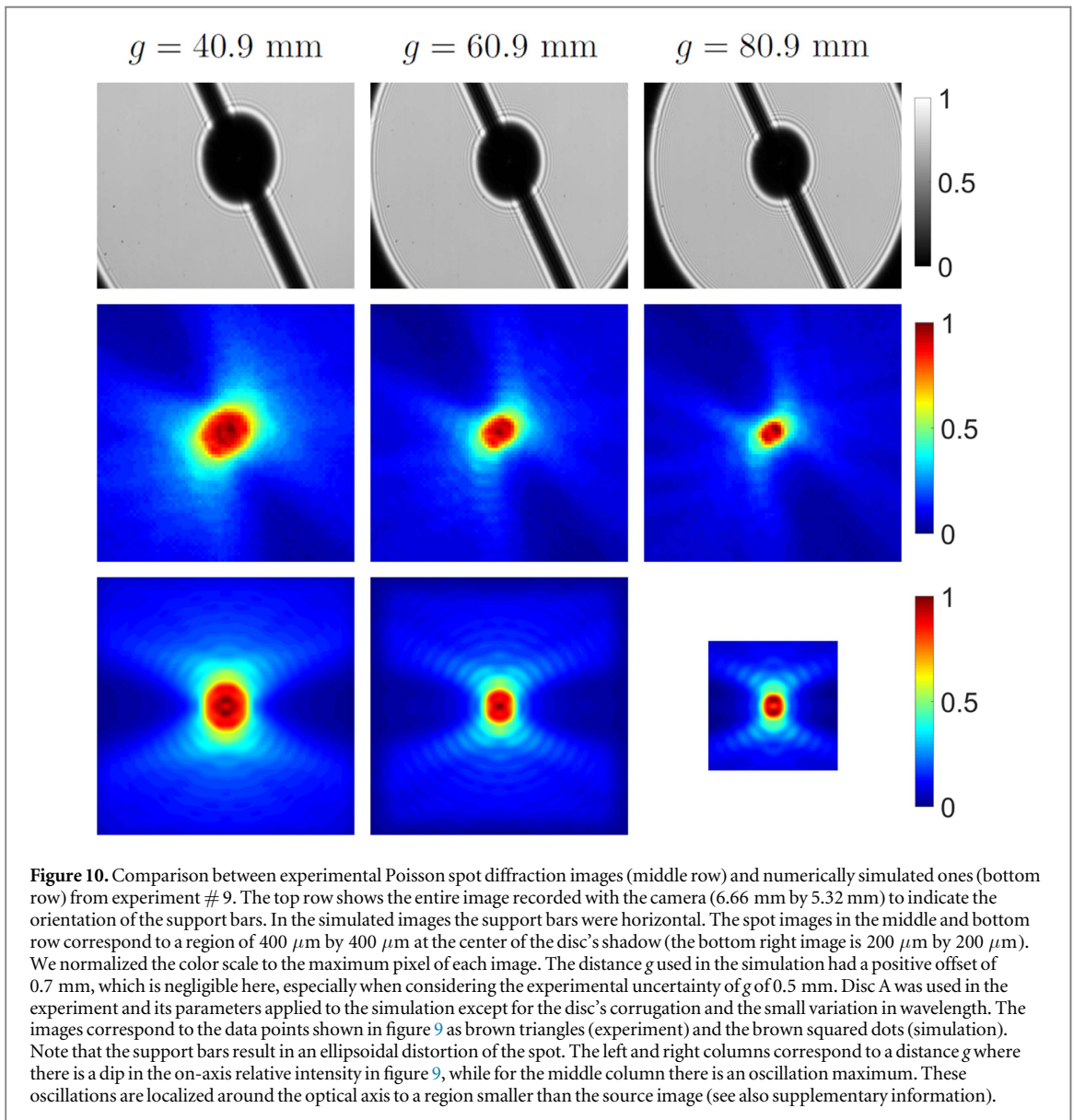
to the previous data sets we varied the detector distance ' $b$ ' instead of ' $g$ ', which better shows the extinction of Poisson's spot due to edge corrugation. Furthermore, in order to increase the sensitivity to edge corrugation we used the blue LED. To better account for variations in the background in these data sets, we additionally subtracted the minimal pixel readout in the geometric shadow of the disc from both the measured on-axis intensity and the measured unobstructed intensity  $I_0$ . Furthermore, the on-axis intensity had to be taken as the maximal pixel intensity within the geometric image of the source, instead of determining the on-axis pixel via the fitting procedure as was done for the other data sets. This was because of the relatively small image widths encountered when reducing  $b$ .

The analytical model accounts for the attenuation of Poisson's spot well. Deviations can be mostly observed at small  $b$ . We expect that the not entirely random nature of the disc edge corrugation is to blame, but it should be also noted that the model is expected to be less accurate for small  $b$ . The analytic model is expected to overestimate the on-axis intensity by as much as 10%, since we neglected the factor  $\frac{b^2}{b^2 + R^2}$  in equation (1). We however observe the opposite trend. It is satisfying though that the experimental data resulted in higher relative intensities in general, since the model assumes a worst case rectangular-shaped corrugation. In figure 12 the corrugation of disc 'D' completely extinguishes Poisson's spot for the data point with the smallest ' $b$ ' as can be seen in the recorded image. The measured relative intensity for that data point is, however, clearly above zero. This is because additional noise from diffraction keeps the on-axis intensity above the background. This at least in part also results in the observed deviations from the model. For the other data sets Poisson's spot could not be completely extinguished due to the experimentally limited closest approach to the camera.

## 6. Discussion

Our main motivation for finding an analytical model for the intensity of Poisson's spot is the prediction of its visibility in matter-wave diffraction experiments. The model will facilitate the choice of source and detection distances as well as sphere diameters for any particular source and detection system. This will allow to determine if Poisson spot experiments are feasible with matter-waves of increasing mass and complexity which aim to test the quantum mechanical super-position principle in systems of increasing macroscopicity [33]. In order to be able to distinguish between particle and wave behavior for matter waves in the Poisson spot interferometer it is important to realize that the attractive Casimir–Polder potential can lead to a classical on-axis bright spot even in the particle picture. For this reason it would be interesting to derive a similar analytic model for the relative intensity predicted classically, to be able to find out in which parameter regimes a clear distinction between particle and wave is possible.

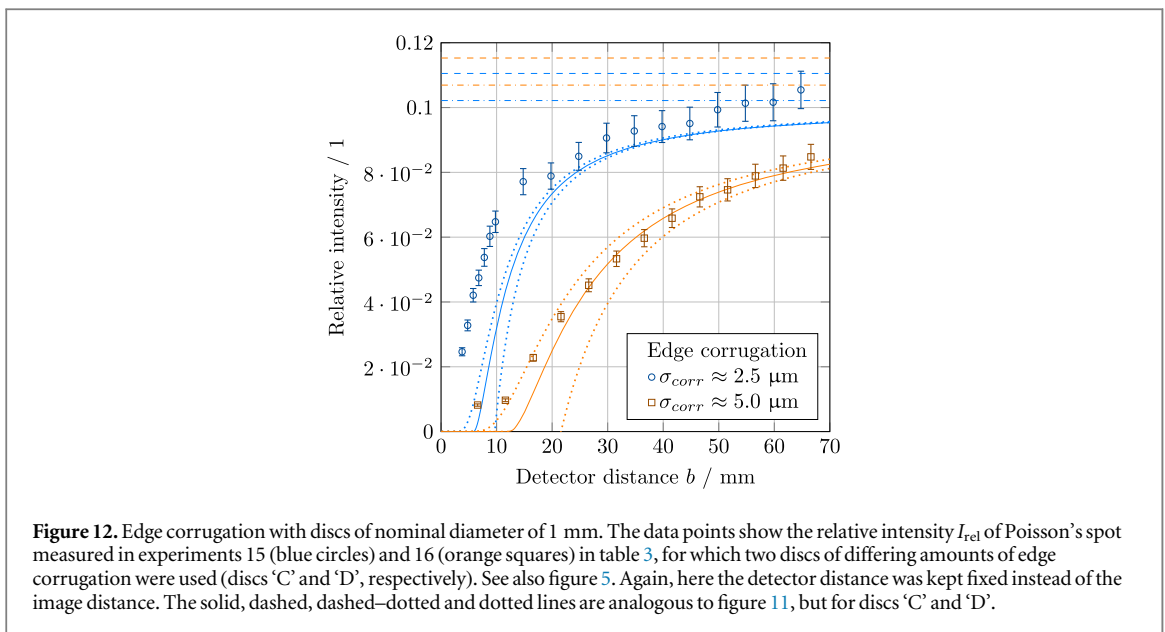
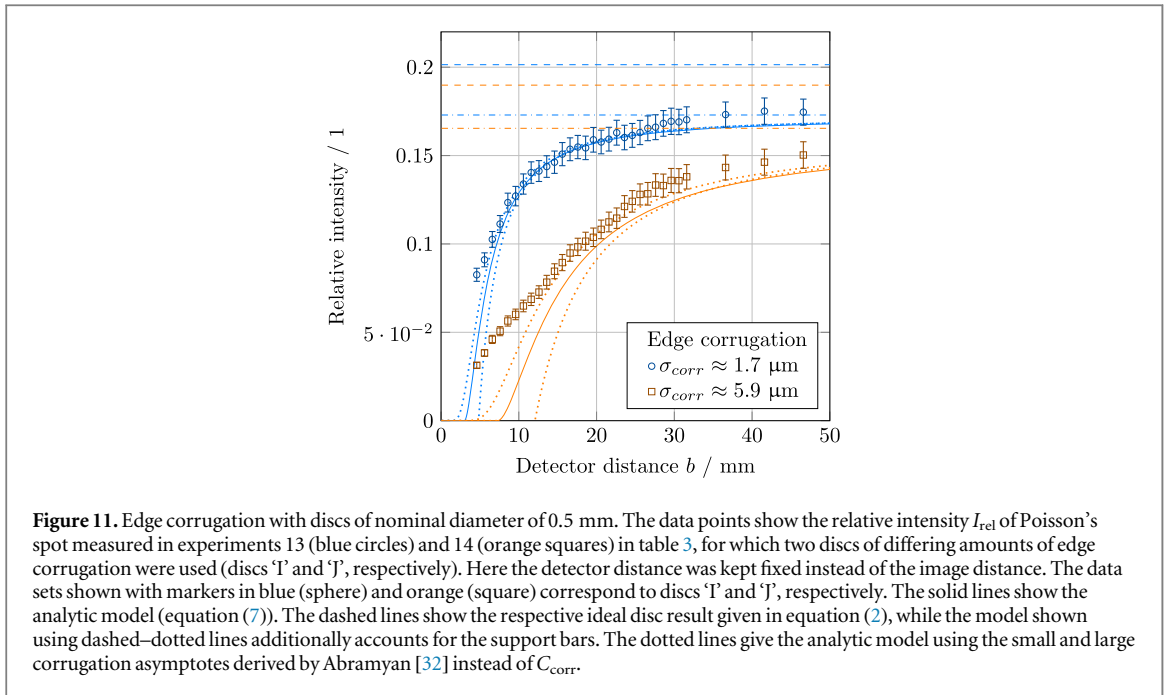
The analytic model will be relevant as well in matter-wave studies as proposed in a recent article, where we discuss the possibility of determining Casimir–Polder forces by measuring  $I_{rel}$  of Poisson's spot in indium matter-wave diffraction experiments [19]. For example, in the article effects from edge corrugation were



neglected, for which equation (6) can be used as good estimate. The Casimir–Polder potential results in an increase of  $I_{\text{rel}}$  close to the disc (small  $b$ ), opposing the effect edge corrugation has. Therefore a clear understanding of the influence of edge corrugation is important in these studies. Finding an analytic approximation of the increase in  $I_{\text{rel}}$  due to the Casimir–Polder potential maybe an interesting further development of the model. Furthermore, the light experiments revealed that care must be taken both with regard to detector resolution and resolution of numerical simulations when comparing theoretical, simulated and experimental on-axis intensities (as for example in figure 6).

The field, also away from the optical axis, behind an opaque disc with random edge roughness was discussed before by Abramyan [32]. There two asymptotic formulae are given, one for the case when the corrugation is large compared to  $w_{\text{fz}}$  and the other when it is small. We have plotted both asymptotes as dotted lines in figures 11 and 12. The prediction from our equation (6) lies between the two asymptotes, as to be expected. The experimental data points, however, do not allow a clear conclusion if equation (6) is more accurate in the intermediate regime, mainly since the particular edge corrugation of the discs is neither purely random nor square-wave shaped. This could be tested in the future, by improving on the fidelity of the edge corrugation of the discs by using higher resolution lithography techniques for the fabrication of the discs.

The effect of surface corrugation also suggests an interesting application for Poisson's spot, as was investigated before [23]. A measurement of the relative intensity of Poisson's spot as a function of distance behind metallic balls, such as used in ball bearings, could be used to estimate their surface quality. In the simple configuration  $g = b = 2 \cdot R$  and using the limit  $r \gg \lambda$  the adjacent Fresnel zone  $w_{\text{fz}}$  is  $\lambda/2$ . Then surface corrugation of the order of  $\lambda/10$  would result in a reduction of  $I_{\text{rel}}$  of about 10%. This could be potentially



measured in a setup of relatively low cost, especially when compared to the optical surface interferometers and stylus profilers commonly used for this purpose [34]. Note, that the factor neglected in equation (1) can no longer be omitted when  $g = b = 2 \cdot R$  and should therefore be included in a fit of experimental data using equation (7) with  $\sigma_{corr}$  as a free parameter. Moreover, under these conditions the plane-wave assumption used to derive this factor is a very crude approximation, so that more considerations will be needed to arrive at an accurate modeling of the Poisson spot intensity for this case. Even though, the Rayleigh–Sommerfeld diffraction integral is expected to be more consistent close to the obscuring disc [35, 36], the Fresnel–Kirchhoff integral may yield a closer agreement with observations of the spot [13, 37].

In the search for extra-terrestrial planets it has been suggested to use a circular mask, a so-called external occulter or star shade, with petal-shaped edge corrugation to block the light from stars in order to be able to detect the many orders of magnitude fainter light reflected by any close-by planets [38, 39]. In analogy to a disc with an apodized transmission function, the petal-shaped edge corrugation efficiently attenuates diffraction into the shadow of a circular disc including Poisson's spot, and thus allows a reduction in the required diameter of the external occulter, reducing its cost. The proposed shape of the corrugation was even shown to be close to optimal

by Vanderbei *et al* [40]. Partial transparency of the petals reduces the requirement of small curvature radii at the petal tips [24, 41]. The analytical model presented here was not aimed at predicting the intensity reductions required in these studies. The rectangular corrugation we assumed only achieves a complete cancellation of Poisson's spot at a particular wavelength and near-perfect corners of the rectangular wave. One point which may be of interest though is that at least in principle an exact measurement of the relative intensity of Poisson's spot from a star may also reveal the presence of a near-by planet (without resolving the two light sources though). This is because the additionally reflected light from the planet reduces the transverse coherence of the incident light. The disc acts in fact analogously to a Michelson stellar interferometer [13], which can be used to measure the angular diameters of near-by stars.

## 7. Conclusion

We have presented an analytical model for the relative on-axis intensity of Poisson's spot, and verified it against a numerical simulation model and experimental data from a light diffraction experiment. The model successfully describes the influence of the most important experimental parameters, namely wavelength, source distance, detector distance, disc radius, edge corrugation and the disc's support structure. Equation (7) that makes up the analytical model can be evaluated fast over a wide range of the parameters, especially when compared to the numerical methods described here. It is thus very useful for finding the optimal parameters or the range of parameters for which the spot can be observed. The model thus forms a good starting point for planning future Poisson-spot experiments. We thus expect that the model will facilitate investigations ranging from Poisson spot lithography [27, 28] to the metrology of the surface corrugation of balls used in bearings [23]. In particular, our planned matter-wave Poisson spot experiments aimed at testing the foundations of quantum-mechanics or measuring the Casimir–Polder interaction will benefit.

## Acknowledgments

We acknowledge fruitful discussions with Stefan Buhmann and Johannes Fiedler (both University of Freiburg, Germany). TR is indebted to Bodil Holst (University of Bergen, Norway) for sparking his initial interest in Poisson's spot and many years of first-rate guidance. TR acknowledges support by the Ministry of Science, Research and Art of Baden-Württemberg via a Research Seed Capital (RISC) grant. TR, PL, HG and HH acknowledge support by the Helmholtz Association. We acknowledge support by Deutsche Forschungsgemeinschaft and Open Access Publishing Fund of Karlsruhe Institute of Technology.

## References

- [1] Hecht E 2002 *Optics* 4th International edn (Reading, MA: Addison-Wesley)
- [2] Fresnel A J 1868 *OEuvres Completes 1* (Paris: Imprimerie impériale)
- [3] Davisson C and Germer L H 1927 Diffraction of electrons by a nickel crystal *Phys. Rev.* **30** 705
- [4] Davisson C and Germer L 1927 Diffraction of electrons by a crystal of nickel *Nature* **119** 558
- [5] Estermann I and Stern O 1930 Beugung von Molekularstrahlen *Z. Phys.* **61** 95–103
- [6] Arndt M, Nairz O, Vos-Andreae J, Keller C, van der Zouw G and Zeilinger A 1999 Wave-particle duality of  $C_{60}$  molecules *Nature* **401** 680–2
- [7] Eibenberger S, Gerlich S, Arndt M, Mayor M and Tüxen J 2013 Matter-wave interference of particles selected from a molecular library with masses exceeding 10 000 amu *Phys. Chem. Chem. Phys.* **15** 14696
- [8] Hackermueller L, Hornberger K, Brezger B, Zeilinger A and Arndt M 2004 Decoherence of matter waves by thermal emission of radiation *Nature* **427** 711–4
- [9] Leggett A J 2005 The quantum measurement problem *Science* **307** 871–2
- [10] Bassi A, Lochan K, Satin S, Singh T P and Ulbricht H 2013 Models of wave-function collapse, underlying theories, and experimental tests *Rev. Mod. Phys.* **85** 471–527
- [11] Nimmrichter S and Hornberger K 2013 Macroscopicity of mechanical quantum superposition states *Phys. Rev. Lett.* **110** 160403
- [12] Sommerfeld A 1978 *Vorlesungen über Theoretische Physik: Optik* vol IV (Frankfurt: Harri Deutsch)
- [13] Born M and Wolf E 1999 *Principles of Optics* (Cambridge: Cambridge University Press)
- [14] Reisinger T, Bracco G and Holst B 2011 Particle-wave discrimination in Poisson spot experiments *New J. Phys.* **13** 065016
- [15] Nowak S, Stuhler N, Pfau T and Mlynek J 1998 Charged wire interferometer for atoms *Phys. Rev. Lett.* **81** 5792–5
- [16] Nimmrichter S 2014 *Macroscopic Matter Wave Interferometry (Springer Theses)* (Berlin: Springer)
- [17] Juffmann T, Nimmrichter S, Arndt M, Gleiter H and Hornberger K 2012 New prospects for de broglie interferometry: grating diffraction in the far-field and Poisson's spot in the near-field *Found. Phys.* **42** 98–110
- [18] Reisinger T, Patel A A, Reingruber H, Fladischer K, Ernst W E, Bracco G, Smith H I and Holst B 2009 Poisson's spot with molecules *Phys. Rev. A* **79** 053823
- [19] Hemmerich J L, Bennett R, Reisinger T, Nimmrichter S, Fiedler J, Hahn H, Gleiter H and Buhmann S Y 2016 Impact of Casimir–Polder interaction on Poisson-spot diffraction at a dielectric sphere *Phys. Rev. A* **94** 023621
- [20] Coulson J and Becknell G G 1922 Reciprocal diffraction relations between circular and elliptical plates *Phys. Rev.* **20** 594–600

- [21] Becknell G G and Coulson J 1922 An extension of the principle of the diffraction evolute, and some of its structural detail *Phys. Rev.* **20** 607–12
- [22] Harvey J E and Forgham J L 1984 The spot of Arago: new relevance for an old phenomenon *Am. J. Phys.* **52** 243
- [23] Kouznetsov D and Lara P 1994 Use of the Poisson point to calibrate balls and rails *Instrum. Desarrollo* **3** 4/1994
- [24] Shiri S and Wasylkiwskyj W 2013 Poisson-spot intensity reduction with a partially transparent petal-shaped optical mask *J. Opt.* **15** 035705
- [25] Sakauchi H and Tsuji R 2009 Compression of Arago spot images for rapid position measurement of inertial fusion energy targets *Plasma Fusion Res.* **4** S1012
- [26] Ovryn B and Hovenac E A 1993 Coherent forward scattering particle-image velocimetry: application of Poisson's spot for velocity measurements in fluids *Proc. SPIE Vol. 2005, Optical Diagnostics in Fluid and Thermal Flow* (International Society for Optics and Photonics) pp 338–48
- [27] Tian S, Xia X, Sun W, Li W, Li J and Gu C 2011 Large-scale ordered silicon microtube arrays fabricated by Poisson spot lithography *Nanotechnology* **22** 395301
- [28] Jung Y, Vacic A, Sun Y, Hadjimichael E and Reed M A 2012 Mapping of near field light and fabrication of complex nanopatterns by diffraction lithography *Nanotechnology* **23** 045301
- [29] Zhang Y, Zhang W, Su M and Chen L 2016 Shaping the Arago–Poisson spot with incomplete spiral phase modulation *J. Opt. Soc. Am. A* **33** 570
- [30] Abramowitz M (ed) 1972 *Handbook of Mathematical Functions: With Formulas, Graphs, and Mathematical Tables* (Dover Books on Advanced Mathematics) (New York: Dover)
- [31] Dager D E 1996 Simulation and study of Fresnel diffraction for arbitrary two-dimensional apertures *Comput. Phys.* **10** 591–604
- [32] Abramyan G L 1981 Theory of the diffraction by an opaque disk with a randomly rough edge *Radiophys. Quantum Electron.* **24** 132–8
- [33] Juffmann T, Ulbricht H and Arndt M 2013 Experimental methods of molecular matter-wave optics *Rep. Prog. Phys.* **76** 086402
- [34] Smith G T 2002 *Industrial metrology—surfaces and roundness* (London: Springer)
- [35] Lucke R L 2006 Rayleigh–Sommerfeld diffraction and Poisson's spot *Eur. J. Phys.* **27** 193–204
- [36] Smith G S 2006 Comment on Rayleigh–Sommerfeld diffraction and Poisson's spot *Eur. J. Phys.* **27** L21–3
- [37] Stammes J J 1986 *Waves in Focal Regions* (Bristol and Boston: Adam Hilger)
- [38] Marchal C 1985 Concept of a space telescope able to see the planets and even the satellites around the nearest stars *Acta Astronaut.* **12** 195–201
- [39] Cash W 2011 Analytic modeling of starshades *Astrophys. J.* **738** 76
- [40] Vanderbei R J, Cady E and Jeremy Kasdin N 2007 Optimal occulter design for finding extrasolar planets *Astrophys. J.* **665** 794
- [41] Wasylkiwskyj W and Shiri S 2011 Limits on achievable intensity reduction with an optical occulter *J. Opt. Soc. Am. A* **28** 1668–76